RSC Advances

PAPER

Check for updates

Cite this: *RSC Adv.*, 2022, **12**, 35064

Enhanced photocatalytic activity of a flower-like $In_2O_3/ZnGa_2O_4$:Cr heterojunction composite with long persisting luminescence†‡

Ailijiang Tuerdi, Peng Yan, Fenggui He and Abdukader Abdukayum *

Received 7th September 2022
Accepted 21st November 2022

DOI: 10.1039/d2ra05646a

rsc.li/rsc-advances

The development of new photocatalysts with high photocatalytic efficiency and catalytic stability, and long persisting luminescence is critical for ensuring environmental protection and clean energy production. In this study, we develop a flower-like $In_2O_3/ZnGa_2O_4$:Cr heterojunction composite with enhanced ultraviolet (UV) photocatalytic activity using a facile two-step hydrothermal method. The spectral response range of the heterojunction composite is widened to the visible-light range owing to the presence of the $ZnGa_2O_4$:Cr persistent luminescence nanoparticles with sizes of less than 10 nm. The heterojunction composite is dispersed on the flower petals of In_2O_3. The $In_2O_3/ZnGa_2O_4$:Cr/1:1 composite exhibits photo-degradation performance for rhodamine B degradation that is superior to those of pure In_2O_3, $ZnGa_2O_4$:Cr, $In_2O_3/ZnGa_2O_4$:Cr/1:0.5 and $In_2O_3/ZnGa_2O_4$:Cr/1:2, achieving complete degradation after 80 min under UV light irradiation. Moreover, it exhibits long afterglow luminescence that lasts for more than 72 h. Thus, the $In_2O_3/ZnGa_2O_4$:Cr/1:1 composite shows great potential for use in round-the-clock photocatalytic applications.

1. Introduction

With rapid economic development, humans have focused their attention on production of colored materials worldwide. This has led to an ongoing increase in the annual output of synthetic dyes. Due to the synthetic dye content in the large amounts of wastewater discharged by dye industries during the production process and the absence of effective treatment, the discharge water harms the environment.[1–3] Photocatalysis technology based on solar energy is a promising approach for the treatment of environmental pollution and for green renewable energy utilization. This technology uses semiconductor photocatalysts that have been investigated in the past several decades. These photocatalysts include TiO_2, CeO_2, g-C_3N_4, ZnO, ZnS, WO_3, In_2O_3, and Bi_2WO_6.[4–11] Among these photocatalysts, as a typical n-type semiconductor photo-catalyst with a band gap of 2.8 eV and outstanding thermodynamic stability,[12] In_2O_3 has drawn significant attention in the studies related to photo-electrochemistry, chemical sensors, photocatalytic hydrogen generation, and the degradation of organic pollutants.[13–16] However, pure In_2O_3 still shows limited photocatalytic activity owing to the fast recombination of the photo-generated electrons and holes and the low utilization of the solar spectrum.[17] Therefore, the construction of heterojunction composites is an effective method to substantially enhance the photocatalytic performance of In_2O_3. For example, heterojunction composites such as $In_2O_3/BiVO_4$, p-CuO–n-In_2O_3, and $ZnFe_2O_4/In_2O_3$ have been rationally designed and exhibit enhanced photocatalytic activity.[18–20] $ZnGa_2O_4$ is an important p-type semiconductor material. It is a blue-emitting phosphor with a wide band gap and a d^{10} electron configuration.[21] $ZnGa_2O_4$ shows great potential for applications in various areas, such as gas sensors, ultraviolet (UV) photodetection, solar energy conversion, and UV light photocatalysis.[22–26] It is an ideal host lattice that can emit near-infrared (NIR) afterglow upon chromium ion (Cr^{3+}) doping. Therefore, Cr^{3+}-doped $ZnGa_2O_4$ exhibits great potential for *in vivo* bio-imaging with a high signal-to-background ratio.[27] Our previous work showed that the Bi^{3+} and Cr^{3+} co-doped $ZnGa_2O_4$ exhibit excellent photocatalytic activity and NIR persistent luminescence owing to an increase in the trap density and a decrease in the band gap that prolong the lifetime of the photo-generated electron–hole pairs and increase visible light absorption.[24]

Zhang *et al.* were the first to achieve an afterglow degradation effect for rhodamine B (RhB) by using a separated long-lasting phosphors layer to excite TiO_2.[28] Many researchers have sought to attain high-efficiency LLP-assisted photocatalyst is using materials such as $CaAl_2O_4$:(Eu,Nd)/$TiO_{2-x}N_y$,[29] $SrAl_2O_4$:Eu^{2+},Dy^{3+}/g-C_3N_4@NH_2-UiO-66,[30] $TiO_2/Sr_4Al_{14}O_{25}$:Eu^{2+},Dy^{3+},[31] $Ca_{12}Al_{14}O_{33}$:Tb^{3+}(Sm^{3+}),[32] (ZnO:Ga_2O_3:$2GeO_2$):Cr^{3+}/TiO_2 and

Laboratory of Xinjiang Native Medicinal and Edible Plant Resources Chemistry, College of Chemistry and Environmental Sciences, Kashi University, Kashi 844000, China. E-mail: abdukadera@sina.com

† Dedicated to the 60th anniversary of Kashi University and the 40th anniversary of chemistry at Kashi University.

‡ Electronic supplementary information (ESI) available. See DOI: https://doi.org/10.1039/d2ra05646a

Zn_2SiO_4:Ga^{3+}.[33,34] However the photocatalytic properties of these materials still need to be improved. We expect that the combination of In_2O_3 and $ZnGa_2O_4$:Cr^{3+} will prolong carrier lifetimes and improve the band gap of the In_2O_3/$ZnGa_2O_4$:Cr heterojunction composite and also will realize a round-the-clock photocatalytic reaction with long persistent luminescence. To the best of our knowledge, no In_2O_3/$ZnGa_2O_4$:Cr-based composites have been reported to date.

Herein, we developed a flower-like In_2O_3/$ZnGa_2O_4$:Cr heterojunction composite with enhanced UV-light photocatalytic activity using a facile two-step hydrothermal method. The spectral response range of the heterojunction composite is widened to the visible light range by the $ZnGa_2O_4$:Cr persistent luminescence nanoparticles (PLNPs) with sizes smaller than 10 nm. The heterojunction composite was dispersed on the flower petals of In_2O_3. The In_2O_3/$ZnGa_2O_4$:Cr composite exhibited high photo-degradation efficiency for RhB degradation that was higher than those of pure In_2O_3 and $ZnGa_2O_4$:Cr, with complete degradation achieved after 80 min under UV light irradiation. Moreover, the In_2O_3/$ZnGa_2O_4$:Cr composite showed long afterglow luminescence that lasted for more than 72 h. Thus, it shows great potential for round-the-clock photocatalytic applications.

2. Experimental

2.1 Materials and reagents

All of the reagents were used as received without further purification. Ga_2O_3 (99.99%), $InCl_3 \cdot 4H_2O$ (99.9%), $Zn(NO_3)_2 \cdot 6H_2O$ (99.99%), $C_2H_6O_2$, $Cr(NO_3)_3 \cdot 9H_2O$ (99.95%), and $C_{12}H_{25}NaSO_4$ were purchased from Aladdin (Shanghai, China). CH_4N_2O, concentrated HNO_3, and aqueous NH_3 (15 wt%) were purchased from Shanghai Chemical Reagent (Shanghai, China). Ultrapure water (ULPHW) was used to prepare all of the solutions and was also used in the photocatalytic tests.

2.2 Preparation of the In_2O_3/$ZnGa_2O_4$:Cr composite

The In_2O_3/$ZnGa_2O_4$:Cr composites were prepared using a two-step hydrothermal method (Fig. 1). First, flower-like In_2O_3 microspheres were synthesized.[28] Then, $InCl_3 \cdot 4H_2O$ (0.391 g), $C_{12}H_{25}NaO_4S$ (1.09 g), and CH_4N_2O (0.4 g) were dissolved in ULPHW (80 mL). Then, the mixture solution was transferred to a Teflon-lined stainless steel autoclave and heated at 120 °C for 12 h. The resulting colloid solution was centrifuged, and white precipitates were obtained. The precipitates were washed with distilled water and ethanol several times and dried in the air. Finally, the dried precipitates were annealed in air at 500 °C for 2 h, and flower-like In_2O_3 microspheres were obtained.

Subsequently, In_2O_3 (100 mg) was dispersed in $C_2H_6O_2$ (10 mL) for 30 min. The mixed solution was stirred at room temperature for 30 min. Then, Ga^{3+} (0.2 mol L^{-1}, 1.99 mL), Zn^{2+} (0.4 mol L^{-1}, 1 mL), and Cr^{3+} (0.01 mol L^{-1}, 0.4 mL) solutions were added to the above mixed solution, and stirred for 30 min. Aqueous NH_3 was added to the mixture to adjust the pH to 9. The resulting mixture was transferred to an autoclave and heated at 170 °C for 24 h. The products were centrifuged.

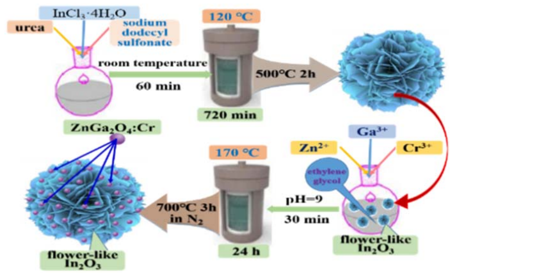

Fig. 1 Schematic of the preparation of the In_2O_3/$ZnGa_2O_4$:Cr composites.

Finally, the sample was annealed at 700 °C in N_2 protection for 3 h. The obtained sample was denoted as the In_2O_3/$ZnGa_2O_4$:Cr/1:1 composite.

2.3 Sample characterization

The X-ray diffraction (XRD) patterns for the obtained samples were recorded using a Bruker D8 Focus Advance X-ray diffractometer (Bruker, Germany) with Cu-Kα radiation (λ = 0.15406 nm). The microstructures and chemical composition were determined using a SU8220 field-emission scanning electron microscope with an EDS spectrometer (Hitachi, Japan). High-resolution transmission electron microscope (HR-TEM) images were obtained using a JEM-2100 HR-TEM microscope (JEOL, Japan). Photoluminescence spectra and persistent luminescence decay curves were obtained using an F-4500 fluorescence spectrophotometer (Hitachi, Japan). Ultraviolet-visible (UV-vis) diffuse reflectance spectra were recorded using a UV-vis spectrophotometer (Shimadzu UV-2600, Japan).

2.4 Photocatalytic activity test

We evaluated the photocatalytic performance of the as-prepared In_2O_3/$ZnGa_2O_4$:Cr composites by measuring the photodegradation efficiency of RhB under UV irradiation by a mercury lamp (300 W, illumination intensity is 8.1346 W cm^{-2}) at room temperature. An In_2O_3/$ZnGa_2O_4$:Cr sample (20 mg) was combined with a 10 mg L^{-1} aqueous RhB solution (40 mL). Magnetic stirring was performed continuously in the dark for 40 min to reach the adsorption–desorption equilibrium. Then, the suspension was placed under UV light irradiation, and the samples were collected, separated, and analyzed with a spectrophotometer at regular time intervals (every 20 min) using the same method.

3. Results and discussion

3.1 Characterization of the crystal structure

The crystal structures of the as-prepared flower-like In_2O_3, $ZnGa_2O_4$:Cr, and In_2O_3/$ZnGa_2O_4$:Cr composites were characterized using XRD. Fig. 2 shows that all of the peaks were assigned to the In_2O_3 sample with the peaks at the 2θ values of 21.47°, 30.59°, 35.47°, 37.58°, 41.49°, 45.64°, 51.06°, 56.08°, and 60.71° indexed to the (211), (222), (400), (411), (332), (431), (440), (611), and (622) cubic In_2O_3 crystal planes, respectively,[35] that

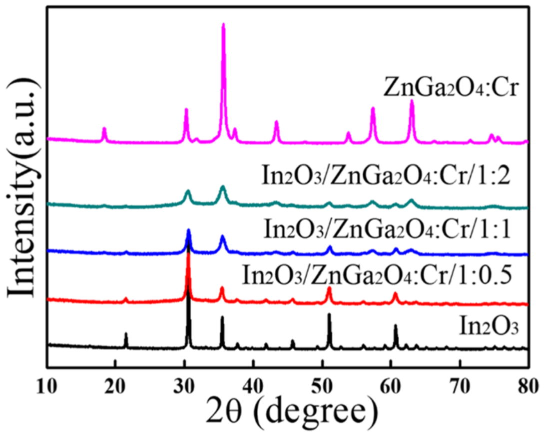

Fig. 2 XRD patterns of the In_2O_3, $ZnGa_2O_4$:Cr, and $In_2O_3/ZnGa_2O_4$:Cr composites.

are consistent with the standard JCPDS pattern (file no.06-0416). Moreover, no impurity diffraction peaks were observed. In the $ZnGa_2O_4$:Cr sample, the peaks were observed at the 2θ of 18.45°, 30.28°, 35.7°, 37.4°, 43.58°, 53.85°, 57.56°, 63.19°, and 74.72°, and all of the diffraction peaks were consistent with the spinel phase of $ZnGa_2O_4$ (file no. 38-1240) and could be indexed as the (111), (220), (311), (222), (400), (422), (511), (440), and (531) crystal planes, respectively.[27] Furthermore, the diffraction peaks of the $In_2O_3/ZnGa_2O_4$:Cr/1:1 heterostructure were similar to the corresponding XRD patterns of cubic In_2O_3 and the spinel phase of $ZnGa_2O_4$. Moreover, with increasing $ZnGa_2O_4$:Cr content, the diffraction peaks of $ZnGa_2O_4$:Cr gradually became stronger than those of In_2O_3. These results revealed that the cubic and spinel phases coexisted, indicating that $In_2O_3/ZnGa_2O_4$:Cr/1:1 heterostructure composites were successfully constructed with $ZnGa_2O_4$:Cr PLNPs with sizes of less than 10 nm dispersed on the flower petals of In_2O_3. Fig. S1‡ shows the diffraction peaks for the samples with the different contents of In_2O_3 and $ZnGa_2O_4$:Cr. No impurity phases were observed.

3.2 Morphology analysis

The morphology and elemental composition of the flower-like In_2O_3, $ZnGa_2O_4$:Cr, and $In_2O_3/ZnGa_2O_4$:Cr/1:1 composites were further investigated using FESEM, TEM, and EDS. The low-magnification FESEM image of In_2O_3 (Fig. 3a) shows that the products consisted of numerous flower-like microspheres with sizes ranging from 2 to 5 μm. Detailed morphology information of In_2O_3 was obtained *via* enlarged magnification FESEM (Fig. 3b) and TEM (Fig. 3c), revealing that these flower-like nanostructures are formed from nanosheets. Notably, the thickness of the flower petals and the edge of the nanosheets is approximately 20 nm, and the as-obtained flower-like structure can generally be classified as a hierarchical structure. The FESEM and TEM images (Fig. 3d and e) of the $In_2O_3/ZnGa_2O_4$:Cr/1:1 composite show that the flower-like structure was preserved. The dark spots observed in the images had a diameter of approximately 10 nm and represented $ZnGa_2O_4$:Cr PLNPs that were well-dispersed on the flower petals of In_2O_3. The HR-TEM and SAED analyses indicated that the $ZnGa_2O_4$:Cr PLNPs had a single-crystal structure and that the distance between the lattice fringes was 0.48 nm (Fig. 3f). This distance corresponds to the *d*-spacing of the $ZnGa_2O_4$(111) lattice planes. Furthermore, the SAED pattern confirmed that the crystals of the $ZnGa_2O_4$:Cr PLNPs were pure spinel crystals. The results of the EDS analysis demonstrated that the flower-like In_2O_3 was composed of only In and O_2 (Fig. 3g) and that the $In_2O_3/ZnGa_2O_4$:Cr/1:1 composite was composed of only In, Ga, Zn, Cr,

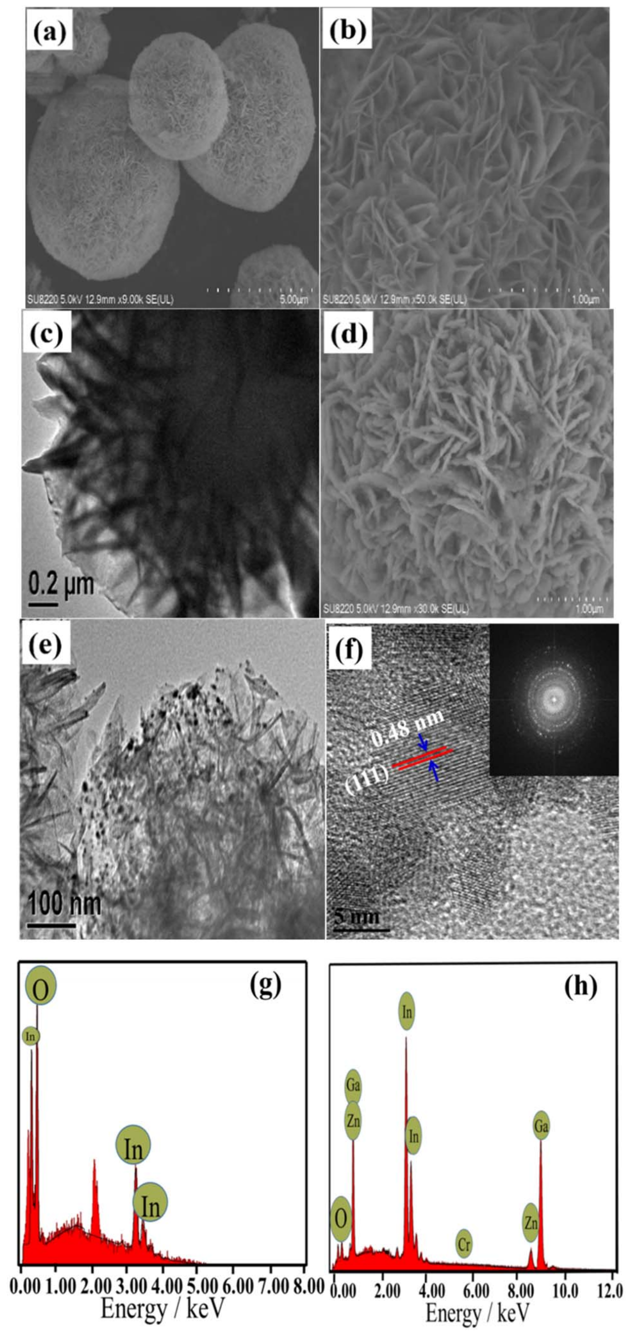

Fig. 3 (a–c) SEM and TEM images of flower-like In_2O_3; (d–f)SEM and TEM, HRTEM, and SAED images of the $In_2O_3/ZnGa_2O_4$:Cr/1:1 composites; EDS patterns of the (g) flower-like In_2O_3 and (h) $In_2O_3/ZnGa_2O_4$:Cr/1:1 composites.

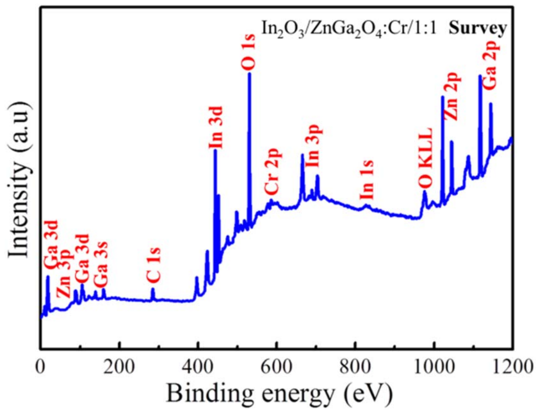

Fig. 4 Survey XPS spectra of the $In_2O_3/ZnGa_2O_4$:Cr/1:1 composites.

and O_2 (Fig. 3h). Moreover, no other elements were found. Using EDS-mapping images, we further confirmed that the In, Ga, O, Zn, and Cr elements were uniformly distributed over the $In_2O_3/ZnGa_2O_4$:Cr composites (Fig. S2‡). These results indicated that the $ZnGa_2O_4$:Cr PLNPs were successfully embedded in the flower petals of In_2O_3 and that the $In_2O_3/ZnGa_2O_4$:Cr/1:1 heterojunction composite was successfully constructed.

To measure the surface chemical composition and the chemical states of the elements, the $In_2O_3/ZnGa_2O_4$:Cr/1:1 composite was characterized by XPS. Peaks of the In, Ga, O, Zn, and Cr and C elements can be observed from the XPS survey spectrum of the $In_2O_3/ZnGa_2O_4$:Cr/1:1 composite (Fig. 4), which is consistent with the EDS analysis results. The peak for C 1s at 284.8 eV is attributed to adventitious hydrocarbon from the XPS instrument.[36] The corresponding high-resolution spectra are also shown in Fig. S3(a and b).‡ The Zn 2p spectrum had two peaks at 1022.28 eV and 1045.35 eV assigned to Zn $2p_{3/2}$ and Zn $2p_{1/2}$, respectively, while the Ga 2p spectrum consisted of the peaks centered at the binding energies of 1118.34 eV and 1145.25 eV that were assigned to Ga $2p_{3/2}$ and Ga $2p_{1/2}$, respectively. These observations demonstrate that Zn and Ga are present in the +2 and +3 oxidization states, respectively. Moreover, the O 1s core level spectrum of the $In_2O_3/ZnGa_2O_4$:Cr composites are shown in Fig. S3c,‡ and the major peaks centered at 529.83, 530.23, and 531.85 eV are attributed to lattice oxygen in the In–O, Zn–O, and Ga–O of $In_2O_3/ZnGa_2O_4$:Cr composites, respectively, whereas the weak peak at 532.17 eV is due to the presence of the surface adsorbed hydroxyl oxygen species.[37–39] The In 3d spectrum also reveals two symmetrical peaks a 444.78 eV (In $3d_{5/2}$) and 452.39 eV (In $3d_{3/2}$) (Fig. S3d‡) that are positively shifted compared to the peaks in pure In_2O_3 (444.3 eV, 451.8 eV), clearly indicating the presence of strong interactions between In_2O_3 and $ZnGa_2O_4$:Cr. This strong electronic interaction is essential for the transfer of the photogenerated charge carriers and the improvement of the photoreactivity.[40,41]

3.3 Optical properties and band structure

The optical absorption of the samples was measured by UV-vis diffuse reflectance spectroscopy (DRS). Fig. 5 shows strong absorption of the flower-like In_2O_3 at less than 500 nm, indicating that light is mostly absorbed in the ultraviolet region, with a band gap $E_g = 2.8$ eV. However, the pure $ZnGa_2O_4$:Cr showed an absorption edge at approximately 350 nm, with a band gap $E_g = 4.5$ eV. Moreover, no light absorption occurred in the visible region. When the flower-like In_2O_3 was combined with the $ZnGa_2O_4$: Cr PLNPs in appropriate proportions (1 : 1), the absorption peaks gradually moved to the visible-light region (with a wavelength of 550 nm). In particular, a red shift of the absorption band edge was distinctly observed for the $In_2O_3/ZnGa_2O_4$:Cr/1:1 composites, and the intensity of the absorption peaks was also significantly enhanced. The band gap or energy gap (E_g) of $In_2O_3/ZnGa_2O_4$:Cr was calculated to be approximately 2.33 eV according to the following equation (Fig. S4‡):[42]

$$\alpha hv = A(hv - E_g)^2 \tag{1}$$

where hv is the photon energy, α is the absorption coefficient, and A is a constant. The narrow band gap of the $In_2O_3/ZnGa_2O_4$:Cr/1:1 composites indicated that the synthesized heterojunction composites can absorb most of the visible light in sunlight. The experimental results demonstrated that the coexisting cubic and spinel phase$In_2O_3/ZnGa_2O_4$:Cr heterojunction composites were successfully constructed using the $ZnGa_2O_4$:Cr particles with the size of 10 nm that were dispersed on the flower petals of In_2O_3. The In_2O_3 played the key roles of an electron carrier and electron acceptor in the $In_2O_3/ZnGa_2O_4$:Cr heterojunction composites. The conduction band (CB) and valence band (VB) of In_2O_3 were located at −0.63 and 2.17 eV, respectively,[35] where as those of $ZnGa_2O_4$:Cr were located at −1.47 and 3.03 eV, respectively.[25] After combining these two semiconductors, $ZnGa_2O_4$:Cr could be excited under UV light, and the electrons generated in $ZnGa_2O_4$:Cr could migrate to the CB of In_2O_3. This process led to decreased electron–hole pair recombination. Subsequently, the electrons transferred to the surface and reacted with O_2 to produce $O_2^{-\bullet}$, thereby oxidizing the organic pollutants.[43] Meanwhile, the abundant holes on the $In_2O_3/ZnGa_2O_4$:Cr surface also

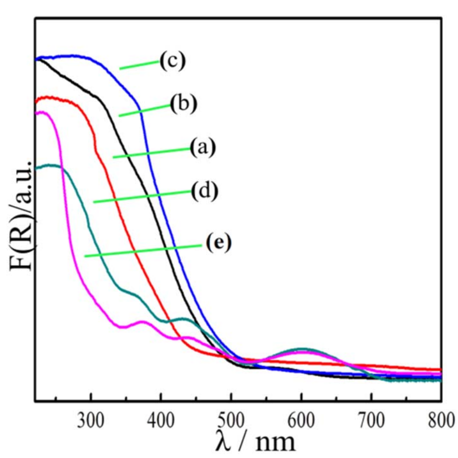

Fig. 5 UV-visible diffuse reflectance spectra of (a) flower-like In_2O_3, (b) $In_2O_3/ZnGa_2O_4$:Cr/1:0.5, (c) $In_2O_3/ZnGa_2O_4$:Cr/1:1, (d) $In_2O_3/ZnGa_2O_4$:Cr/1:2 and (e) $ZnGa_2O_4$:Cr.

participate in the mineralization of the organic pollutants *via* photocatalytic reactions. Therefore, the $In_2O_3/ZnGa_2O_4$:Cr composite photocatalyst showed high photocatalytic activity for the degradation of organic pollutants.

3.4 Photocatalytic activity and mechanism

The photocatalytic activities of the $In_2O_3/ZnGa_2O_4$:Cr composites were evaluated *via* the degradation of RhB molecules under UV light irradiation. First, we established an adsorption–desorption equilibrium between the catalyst and dye molecules and stirred the suspension in the dark for 40 min. Fig. 6 shows that although pure $ZnGa_2O_4$:Cr shows no adsorption, both In_2O_3 and $In_2O_3/ZnGa_2O_4$:Cr have good surface adsorption properties. However, In_2O_3 is preferred to $In_2O_3/ZnGa_2O_4$:Cr because the flower-like In_2O_3 has a large specific surface area.[44] Next, the samples were placed under UV irradiation by a mercury lamp at room temperature. $In_2O_3/ZnGa_2O_4$:Cr/1:1 exhibited good photocatalytic performance with a degradation efficiency of 98.8% after 80 min of irradiation with UV light. The experimental results indicated that the photocatalytic activity of $In_2O_3/ZnGa_2O_4$:Cr/1:1 was higher than that of the pure In_2O_3, $ZnGa_2O_4$:Cr, $In_2O_3/ZnGa_2O_4$:Cr/1:0.5 and $In_2O_3/ZnGa_2O_4$:Cr/1:2 samples that showed the degradation efficiencies of 59.3%, 33.2%, 86.7%, and 50.04%, respectively (Fig. 6). Under UV irradiation, the photo-degradation efficiency of $In_2O_3/ZnGa_2O_4$:Cr/1:1 for RhB was higher than that of other PLNPs in the literature (Table S1‡). The results indicate that the composite with the optimal $In_2O_3/ZnGa_2O_4$: Cr ratio of 1 : 1 shows good photocatalytic activity, while the photocatalytic activity decreases when the composite ratio is greater or lower than the optimal. This phenomenon has been extensively studied in type II heterostructures[45–48] and non-metal and transition metal doped semiconductor systems,[49,50] and is consistent with the interfacial charge transfer mechanism.

The surface-decorated $ZnGa_2O_4$:Cr in the $In_2O_3/ZnGa_2O_4$:Cr/1:1 composite acts as an efficient electron scavenger for In_2O_3, because its conduction band potential (−1.47 V *vs.* NHE) is lower than the CB level of In_2O_3 (−0.63 V *vs.* NHE). Consequently, the photo-excited electrons of $ZnGa_2O_4$:Cr were preferentially transported to In_2O_3, and suppressed charger combination in $ZnGa_2O_4$:Cr, providing abundant charge carriers and leading to the highest photocatalytic activity.[25,35] Therefore, both the co-existing cubic and spinel phase $In_2O_3/ZnGa_2O_4$:Cr/1:1 heterojunction composites not only had good surface adsorption properties but also generated more electron–hole pairs. Subsequently, these electrons transferred to the surface of the composites, thus inhibiting the recombination of the photo-generated electron–hole pairs.

The recyclability of the$In_2O_3/ZnGa_2O_4$:Cr/1:1 nanocomposites for photocatalytic RhB degradation was evaluated by five replicate experiments, as presented in Fig. S5,‡ showing that $In_2O_3/ZnGa_2O_4$:Cr/1:1 maintained more than 89% of its initial photocatalytic activity after five cycles. However, the XRD patterns and XPS spectra of $In_2O_3/ZnGa_2O_4$:Cr/1:1 did not show any notable differences before and after the photocatalytic cycles (Fig. S6 and S7‡). These results indicate that the $In_2O_3/ZnGa_2O_4$:Cr/1:1 composite maintains a favorable chemical state and crystal structure and is not photo-corroded.

The photocatalysis proceeded smoothly, as shown in Fig. 7. When the $In_2O_3/ZnGa_2O_4$:Cr composites were irradiated by UV light, the electrons generated in $ZnGa_2O_4$:Cr migrate to the CB of In_2O_3. This contributed to decreasing the electron–hole pair recombination. Furthermore, the generated electrons and holes are subsequently transferred to the surface of the composites. This process is favorable for electron–hole pair separation. The electrons subsequently transfer to the surface and react with oxygen to produce $O_2^{-\bullet}$.[51] Then, the holes are captured by the hydroxyl groups (HO−) at the surface of the composites and produce hydroxyl radicals ($HO^\bullet$).[20–23] The obtained $O_2^{-\bullet}$ and $HO^\bullet$ are strong oxidizing agents that degrade the RhB molecules. The mechanism of the photo-degradation reaction (Fig. 7) can be represented as follows:[42]

$$In_2O_3/ZnGa_2O_4{:}Cr + h\nu \rightarrow h_{VB}^{+} + e_{CB}^{-} \quad (2)$$

$$h_{VB}^{+} + H_2O \rightarrow {}^{\bullet}HO + H^{+} \quad (3)$$

$$e_{CB}^{-} + O_2 \rightarrow O_2^{-\bullet} \quad (4)$$

$$O_2^{-\bullet} + H^{+} \rightarrow HO_2^{\bullet} \quad (5)$$

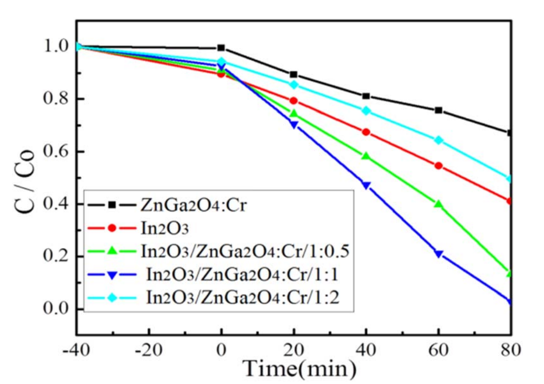

Fig. 6 Photo-degradation efficiency of $In_2O_3/ZnGa_2O_4$:Cr composites.

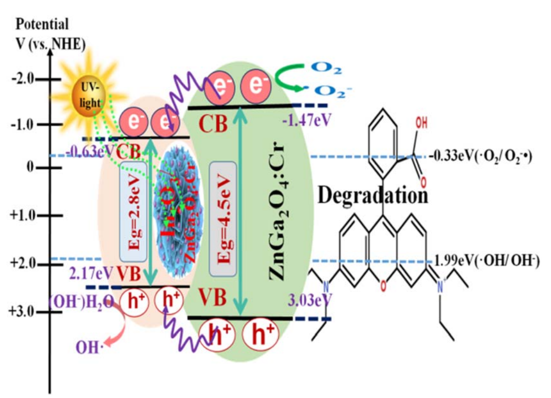

Fig. 7 Schematic illustration of the photocatalytic mechanism of $In_2O_3/ZnGa_2O_4$:Cr composites.

$$\text{Dye} + (^{\bullet}\text{HO}/O_2^{-\bullet}) \rightarrow \text{degradation} \quad (6)$$

3.5 Photoluminescence analyses

Fig. 8 shows the emission spectra of In_2O_3, $ZnGa_2O_4$:Cr, and $In_2O_3/ZnGa_2O_4$:Cr composites at an excitation wavelength of 254 nm. The $ZnGa_2O_4$:Cr and $In_2O_3/ZnGa_2O_4$:Cr composites give a NIR emission band peaking at 698 nm (assigned to the $^2E \rightarrow {}^4A_2$ transition of Cr^{3+}) that is superimposed on a broad emission band in the 600–800 nm range (the $^4T_2 \rightarrow {}^4A^2$ transition of disordered Cr^{3+}).[52] However, no NIR emission band peaks were observed for the pure flower-like In_2O_3. Moreover, the band peak intensity increased as the $ZnGa_2O_4$:Cr content increased from 0.5 to 2. Notably, the composite with the appropriate proportions of In_2O_3 and $ZnGa_2O_4$:Cr ($In_2O_3/ZnGa_2O_4$:Cr/1:1) also showed a certain intensity of NIR emission band peaks. The results demonstrated that the co-existing cubic and spinel phase $In_2O_3/ZnGa_2O_4$:Cr heterojunction composites accelerated electron transfer and were favorable for the separation of electron–hole pairs. Moreover, they showed a strong emission spectrum in the NIR. The photoluminescence excitation spectrum was monitored at 696 nm. Four main absorption bands were observed (Fig. S8‡). The strong band peak at approximately 260 nm was most likely due to the combination of the O–Cr charge transfer band and the $ZnGa_2O_4$ host excitation band.[26] The bands had peaks at approximately 413, 473, and 555 nm and originated from the $^4A_2 \rightarrow {}^4T_1$ (te^2), $^4A_2 \rightarrow {}^4T_1$ (te^2), and $^4A_2 \rightarrow {}^4T_2$ (te^2) transitions that were assigned to the 3d intra-shell transitions of Cr^{3+}, respectively.[19]

Fig. 9a shows the NIR afterglow decay curve of $In_2O_3/ZnGa_2O_4$:Cr monitored at 698 nm following excitation by 254 nm UV light for 5 min. The data were recorded for 20 min. Significant persistent luminescence signals could still be observed with the naked eye after 20 min. The decay curves of the NIR afterglow can be fitted well using the following three-exponential equation:[53]

$$I(t) = I_0 + A_1 e^{-t/\tau_1} + A_2 e^{-t/\tau_2} + A_3 e^{-t/\tau_3} \quad (7)$$

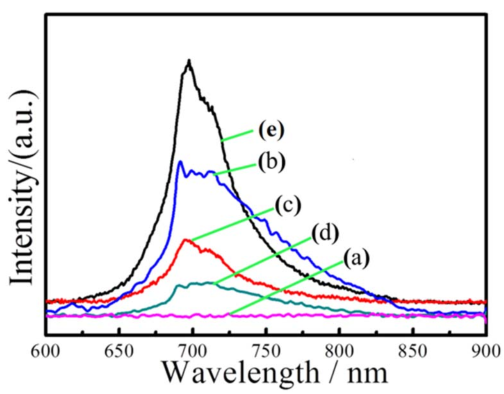

Fig. 8 Emission spectra of (a) flower-like In_2O_3, (b) $In_2O_3/ZnGa_2O_4$:Cr/1:2, (c) $In_2O_3/ZnGa_2O_4$:Cr/1:1, (d) $In_2O_3/ZnGa_2O_4$:Cr/1:0.5 and (e) $ZnGa_2O_4$:Cr.

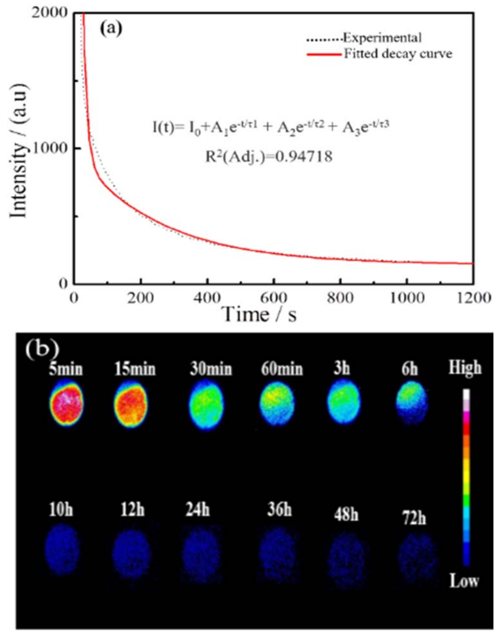

Fig. 9 (a and b) NIR afterglow decay curve and NIR afterglow images of the $In_2O_3/ZnGa_2O_4$:Cr/1:1 at different times.

where I_0 is the initial intensity of the afterglow; $I(t)$ is the intensity of the afterglow at time t; A_1, A_2, and A_3 are constants; and τ_1, τ_2, and τ_3 are the derived lifetimes for the exponential components corresponding to the three different decay processes. Table S2‡ shows the fitting results obtained using the above formula. The average photoluminescence lifetime (τ_{av}) was 27.97 s. This result indicated that $In_2O_3/ZnGa_2O_4$:Cr had a long photoluminescence lifetime. We investigated the persistent luminescence decay of the $In_2O_3/ZnGa_2O_4$:Cr composite using a charge-coupled device camera at different times (10 min) of irradiation with 254 nm UV light. We still detected a non-negligible NIR luminescence signal (SNR = 3.1) from the $In_2O_3/ZnGa_2O_4$:Cr 72 h after stopping the UV irradiation (Fig. 9b). This phenomenon indicates that the as-prepared composites exhibit great potential for round-the-clock photocatalytic applications.

4. Conclusions

A flower-like $In_2O_3/ZnGa_2O_4$:Cr/1:1 heterojunction composite with long NIR persistent luminescence was synthesized using an ethylene glycol-assisted hydrothermal method. The photocatalytic activity of the $In_2O_3/ZnGa_2O_4$:Cr composite was improved *via* the dispersion of the $ZnGa_2O_4$:Cr PLNPs on the flower petals of In_2O_3. The as-prepared $In_2O_3/ZnGa_2O_4$:Cr/1:1 composite exhibited good photocatalytic activity for RhB degradation, with a degradation efficiency of 98.8% after 80 min under UV light irradiation, which is higher than those of the pure In_2O_3, $ZnGa_2O_4$:Cr, $In_2O_3/ZnGa_2O_4$:Cr/1:0.5, and $In_2O_3/ZnGa_2O_4$:Cr/1:2 nanoparticles. Moreover, the composite exhibited long afterglow luminescence that lasted more than 72 h. Thus, the $In_2O_3/ZnGa_2O_4$:Cr composite shows great potential for use in round-the-clock photocatalytic applications.

Author contributions

Ailijiang Tuerdi: conceptualization, methodology, investigation, writing – original draft. Peng Yan: investigation. Fenggui He: investigation. Abdukader Abdukayum: conceptualization, methodology, project administration, resources, supervision, funding acquisition, writing – review & editing.

Conflicts of interest

There are no conflicts to declare.

Acknowledgements

This work is supported by the Scientific Research Program of the Higher Education Institution of Xinjiang (XJEDU2018I017), the Natural Science Foundation of Xinjiang Uygur Autonomous Region (2022D01E16), and Applied Technology Research and Development Program of Kashi Region (KS2020027).

Notes and references

1 S. Papic, N. Koprivanac, A. L. Bozic and A. Metes, *Dyes Pigm.*, 2004, **62**, 291–298.
2 A. Latif, S. Noor, Q. M. Sharif and M. Najeebullah, *J. Chem. Soc. Pak.*, 2010, **32**, 115–124.
3 T. B. Zanoni, M. Tiago, F. Faiao-Flores, S. B. de Moraes Barros, A. Bast, G. Hageman, D. P. de Oliveira and S. S. Maria-Engler, *Toxicol. Lett.*, 2014, **227**, 139–149.
4 H. Xu, S. Ouyang, L. Liu, P. Reunchan, N. Umezawa and J. Ye, *J. Mater. Chem. A*, 2014, **2**, 12642–12661.
5 W. Lei, T. Zhang, L. Gu, P. Liu, J. A. Rodriguez, G. Liu and M. Liu, *ACS Catal.*, 2015, **5**, 4385–4393.
6 N. Ding, X. Chang, N. Shi, X. Yin, F. Qi and Y. Sun, *Environ. Sci. Pollut. Res.*, 2019, **26**, 18730–18738.
7 Z. Wu, L. Na and D. Zhang, *J. Porous Mater.*, 2014, **21**, 157–164.
8 W. Zeng, Y. Ren, Y. Zheng, A. Pan and T. Zhu, *ChemCatChem*, 2021, **13**, 564–573.
9 L. Yang, X. Xiao, R. Zuo, Y. Lin and S. You, *Mater. Sci. Forum*, 2020, **993**, 893–898.
10 L. Chuan, M. Tian, J. Wang, J. Wang, J. C. Yu and S. Yu, *J. Catal.*, 2013, **310**, 84–90.
11 X. Zhang, S. Yu, Y. Liu, Q. Zhang and Y. Zhou, *Appl. Surf. Sci.*, 2017, **396**, 652–658.
12 L. Chen and W. Zhang, *Appl. Surf. Sci.*, 2014, **301**, 428–435.
13 Z. Lei, F. Yang, C. Yuan, L. Tai, C. Yao and D. Fang, *Nano*, 2021, **16**, 2150018.
14 D. Wei, W. Jiang, H. Gao, X. Chuai, F. Liu, F. Liu, P. Sun, X. Liang, Y. Gao, X. Yan and G. Lu, *Sens. Actuators, B*, 2018, **276**, 413–420.
15 M. Liu, P. Li, S. Wang, Y. Liu and H. Sun, *J. Colloid Interface Sci.*, 2021, **587**, 876–882.
16 H. Xu, Y. Wang, X. Dong, N. Zheng and X. Zhang, *Appl. Catal., B*, 2019, **257**, 117932.
17 J. Mu, C. Shao, Z. Guo, M. Zhang and Y. Liu, *J. Mater. Chem.*, 2011, **22**, 1786–1793.
18 J. Yin, S. Huang, Z. Jian, M. Pan, Y. Zhang, Z. Fei and X. Xu, *Appl. Phys. A*, 2015, **120**, 1529–1535.
19 C. Zhang, Y. Huan, D. Sun and Y. Lu, *J. Alloys Compd.*, 2020, **842**, 155857.
20 F. Zhang, X. Li, Q. Zhao and D. Zhang, *ACS Sustainable Chem. Eng.*, 2016, **4**, 4554–4562.
21 L. Tien, C. Tseng, Y. Chen and C. Ho, *J. Alloys Compd.*, 2013, **555**, 325–329.
22 J. Gil-Rostra, F. Valencia and A. González-Elipe, *J. Lumin.*, 2020, **228**, 117617.
23 A. Abdukayum, C. Yang, Q. Zhao, J. Chen and X. Yan, *Anal. Chem.*, 2014, **86**, 4096–4101.
24 A. Tuerdi and A. Abdukayum, *RSC Adv.*, 2019, **9**, 17653–17657.
25 X. Yang, J. Ma, R. Guo, X. Fan, P. Xue, X. Wang, H. Sun, Q. Yang and X. Lai, *Mater. Chem. Front.*, 2021, **5**, 5790–5797.
26 V. Munusami, K. Arutselvan and S. Vadivel, *Diamond Relat. Mater.*, 2020, **111**, 108167.
27 B. S. Bhupendra, K. Anxiu and Y. Mao, *Chem. Commun.*, 2015, **51**, 7372–7375.
28 J. Y. Zhang, F. Pan, W. C. Hao, Q. Ge and T. M. Wang, *Appl. Phys. Lett.*, 2004, **85**, 5778–5780.
29 H. H. Li, S. Yin and T. Sato, *Appl. Catal., B*, 2011, **106**, 586–591.
30 M. L. Chen, S. S. Li, L. Wen, Z. Xu, H. H. Li, L. Ding and Y. H. Cheng, *J. Colloid Interface Sci.*, 2023, **629**, 409–421.
31 H. J. Sung, S. C. Jung and J. S. Kim, *J. Nanosci. Nanotechnol.*, 2021, **21**, 3729–3734.
32 R. Liu, Y. S. Yan and C. C. Ma, *Front. Chem.*, 2018, **6**, 69–78.
33 F. Locardi, E. Sanguineti, M. Fasoli, M. Martini, G. A. Costa, M. Ferretti and V. Caratto, *Catal. Commun.*, 2016, **74**, 24–27.
34 J. J. Zhou, J. Huang, Y. Xia, H. Ou and Z. J. Li, *Sci. Total Environ.*, 2019, **6**, 134342–134347.
35 B. Han, J. Wang, W. Yang, X. Chen and X. Wei, *Sens. Actuators, B*, 2020, **309**, 127788.
36 S. Gao, C. Dong, L. Hong, K. Xiao, X. Pan and X. Li, *Electrochim. Acta*, 2013, **114**, 233–241.
37 S. Zhao, Y. B. Shen, P. F. Zhou, F. L Hao, X. Y. Xua, S. L. Gaoa, D. Z. Wei, Y. X. Ao and Y. S. Shen, *Sens. Actuators, B*, 2020, **308**, 127729–127738.
38 I. Lopez, A. D. Utrilla, E. Nogales, B. I. Mendez and J. Piqueras, *J. Phys. Chem. C*, 2012, **116**, 3935–3943.
39 L. Yang, Y. Z. Hong, E. Liu, X. Zhang, L. Y. Wang, X. Lin and J. Y. Shi, *Sep. Purif. Technol.*, 2021, **263**, 118366–118376.
40 Q. Zhu, Y. K Sun, S. Xu, Y. L Li, X. L. Lin and Y. L. Qin, *J. Hazard. Mater.*, 2020, **382**, 121098–121101.
41 Y. J. Chen, G. H. Tian, Z. Y. Ren, K. Pan, Y. H. Shi, J. Q. Wang and H. G. Fu, *ACS Appl. Mater. Interfaces*, 2014, **6**, 13841–13849.
42 A. Tuerdi, A. Abdukayum and C. Pei, *Mater. Lett.*, 2017, **209**, 235–239.
43 Q. Li, L. Zhang, C. Tang, P. Zhao and J. Yin, *Int. J. Hydrogen Energy*, 2020, **45**, 6621–6628.

44 G. Zhu, M. Hojamberdiev, K. I. Katsumata, N. Matsushita, K. Okada, P. Liu and J. Zhou, *Adv. Mater. Res.*, 2013, **747**, 635–638.
45 C. W. Tsao, M. J. Fang and Y. J. Hsu, *Coord. Chem. Rev.*, 2021, **438**, 213876–213905.
46 T. H. Lai, K. I. Katsumata and Y. J. Hsu, *Nanophotonics*, 2020, **10**, 777–795.
47 Y. H. Chiu, T. M. Chang, C. Y. Chen, M. Sone and Y. J. Hsu, *Catalysts*, 2019, **9**, 430–445.
48 Y. F. Lin and Y. J. Hsu, *Appl. Catal., B*, 2013, **130**, 93–98.
49 S. Lee, Y. Lee and G. N. Panin, *ACS Appl. Mater. Interfaces*, 2017, **5**, 1557–1577.
50 M. J. Fang, C. W. Tsao and Y. J. Hsu, *J. Phys. D: Appl. Phys.*, 2020, **53**, 143001–143032.
51 M. Elavarasan, K. Uma and K. Yan, *J. Taiwan Inst. Chem. Eng.*, 2021, **120**, 169–177.
52 A. Abdukayum, A. Tuerdi, R. Abdurahman, M. Tursun and N. Nurmat, *J. Inorg. Mater.*, 2016, **31**, 1363–1369.
53 A. Abdukayum, J. Chen, Q. Zhao and X. Yan, *J. Am. Chem. Soc.*, 2013, **135**, 14125–14133.